Computational Materials Science 125 (2016) 309–318

Contents lists available at ScienceDirect

Computational Materials Science

journal homepage: www.elsevier.com/locate/commatsci

# Microstructure modeling of random composites with cylindrical inclusions having high volume fraction and broad aspect ratio distribution

Mohammad Islam [a], Gregory J. Tudryn [b], Catalin R. Picu [a,*]

[a] Department of Mechanical, Aerospace and Nuclear Engineering, Rensselaer Polytechnic Institute, Troy, NY 12180, USA
[b] Ecovative Design LLC, Green Island, NY 12183, USA

ARTICLE INFO

*Article history:*
Received 31 May 2016
Received in revised form 29 August 2016
Accepted 30 August 2016

*Keywords:*
Microstructure modeling
Random inclusion composites
Dynamic packing simulation

ABSTRACT

This paper presents a computational methodology for generating microstructure models of random composites with cylindrical or sphero-cylindrical inclusions having high volume fraction and broad aspect ratio distribution. The proposed methodology couples the random sequential adsorption (RSA) algorithm and dynamic finite element (FE) simulations. It uses RSA to generate sparse inclusion assemblies of low volume fraction and subsequently utilizes dynamic FE simulation for inclusion packing to achieve high volume fractions. The method can generate RVEs with volume fraction as high as 50% depending on the inclusion aspect ratio. Its capability is demonstrated by generating three distinct types of models with different inclusion characteristics which are further characterized in terms of homogeneity and isotropy. The results indicate that the proposed method is capable of generating models with low spatial variability of the filler orientation and volume fraction. The method can be used to generate input configurations for continuum and discrete representations of such random media.



## 1. Introduction

Macroscopic properties of inclusion-reinforced composites predominantly depend on the material microstructure. Particulate composites are usually random both in terms of the position of inclusions and their orientation (if non-spherical). While the mean filling volume fraction is defined, a non-uniform spatial distribution of inclusions may exist. Likewise, inclusions may have different morphologies and/or spatial orientation. Such variability has a rather small effect on the overall composite behavior, but has a large influence on the local field fluctuations, hence being of key importance for the prediction of damage nucleation and evolution.

A number of analytical and experimental methods have been developed in the literature to evaluate composite properties. Relevant reviews are presented in Refs. [1–3]. Many analytical models have been developed either based on Eshelby's strain tensor [4,5] or based on other micromechanics results [6,7]. Analytical methods were originally developed for unidirectional fiber reinforced composites and then modified to take into account random fiber orientation via tensor averaging [8] or classical lamination theory [9]. These models provide only bounds of the homogenized composite behavior because the microstructure of the composite is not represented in detail [10].

For random inclusion composites of high volume fraction, numerical modeling techniques, such as the finite element method (FEM), provide clear advantages. Finite element models represent microstructural details more effectively, and implicitly capture the field-mediated interaction of inclusions, which is usually represented only in the mean field sense in analytical models. Such simulations are performed using a statistically representative volume element (RVE) which is used to evaluate the average (homogenized) material properties. The RVE is the smallest volume over which a measurement can be made that yields a value representative of the composite behavior [11]. In order for a sample to be statistically representative, it should be large enough and should contain sufficient number of inclusions. The minimum size of the RVE is determined numerically by considering a sequence of models of increasing size.

Numerical generation of 3D RVEs for random inclusion composites (RIC) is inherently a challenging task [12]. For composites with periodic microstructure the periodic unit cell of the material can be chosen as RVE and the size of the model is dictated by the period of the microstructure. If no such internal characteristic length exists, the RVE size has to be determined numerically. To be statistically

* Corresponding author.
*E-mail address:* picuc@rpi.edu (C.R. Picu).

http://dx.doi.org/10.1016/j.commatsci.2016.08.051
0927-0256/

representative, such RVEs should contain sufficient information about the inclusion size, aspect ratio, orientation and spatial distribution. As the filler volume fraction and/or their aspect ratio increase, generating representative composite models becomes progressively more difficult. The prevalent method to generate such models is random sequential adsorption (RSA) [12–18]. In RSA inclusions are sequentially deposited in a box of desired size such that no two inclusions intersect and the distance between any two inclusions is always larger than a pre-defined threshold. The algorithm stops when the desired volume fraction is achieved or when no more inclusions can be added due to overlaps. Bohm et al. [16] implemented RSA to generate models of metal matrix composites with cylindrical or spheroidal fillers. They used 15 identical fibers with constant aspect ratio (AR) of 5 and achieved a volume fraction equal to 15%. Pan et al. [13] applied a modified RSA algorithm for a random fiber composite with fiber AR = 10 and achieved 13.5% volume fraction. Kari et al. [17] used a similar algorithm to generate models of randomly distributed short fiber and transversely randomly distributed short fiber composites with various volume fractions and aspect ratios.

The major issue with RSA-type methods is the existence of a geometrical jamming limit beyond which no additional inclusions can be added without overlap. This limits the volume fraction that can be reached [19]. Kari et al. [17] reported that the RSA algorithm cannot generate volume fractions larger than 25% for aspect ratios in the range $1 < AR \leqslant 10$. Several other authors also discussed the jamming limit, and the maximum achievable volume fraction has been similarly reported to be 20–25%, depending on the aspect ratio. To achieve higher volume fractions, Kari et al. [17] used different sizes of inclusions and deposited them in the descending order of their size. With this approach, they could achieve volume fractions up to 40%. However, this method is not applicable if all inclusions have the same aspect ratio. It also imposes limitations with respect to the distribution of filler size. Pan et al. [18] and Baliakanavar et al. [14] introduced local filler curvatures at points where sequentially deposited fillers overlap, in order to avoid their intersection and to reduce the algorithmic rejection rate at the same time. A volume fraction of about 35–45% has been reported for models with planar filler orientation. However, the local curvature introduced in the fillers leads to local stress concentration and the algorithm is inherently computation expensive because numerous filler intersection check-adjust loops must be executed.

This literature review indicates that currently available numerical tools lack the capability of generating microstructure models of RICs with high volume fraction at relatively low computational cost. In addition, it is important to develop numerical tools capable of generating models with realistic microstructural details. As mentioned above, a predefined constant gap is introduced between fillers in the RSA algorithm. This is arbitrary since in real materials the gap between two neighboring inclusions is entirely random. This limits the ability of the model to accurately predict the local stress state. Pan et al. [13] studied the effect of the gap size between two fillers embedded in a matrix. They found that the local stress concentration increases as the gap between fillers decreases and the effect becomes more pronounced at high volume fractions. In the present work we address these key issues.

This article presents a novel numerical method for generating RVEs of composites with randomly distributed inclusions. The proposed approach efficiently integrates the widely used RSA algorithm with dynamic FEM in order to generate composite models. Integration of dynamic FEM with RSA provides two distinct advantages. Firstly, it allows generate high volume fraction of inclusions. Secondly, inclusions can be packed more efficiently using this approach while satisfying the non-overlapping constraint. To overcome the jamming limit characteristic for RSA, we avoided generating inclusions in the actual composite domain in the first attempt. Rather we generate sparse and non-overlapping filler assemblies with low volume fraction in six pseudo-composite boxes surrounding the target box. Next, we perform a dynamic FE simulation based on transient dynamic FEM to push all inclusions into the target model box. Hence, all inclusions are packed simultaneously, which differs from iterative packing methods. Furthermore, a surface-to-surface based contact algorithm is used to prevent inclusion overlapping during packing. Contacts between inclusions are automatically detected and these are relocated accordingly to avoid intersection. The proposed method offers the following features that are superior to existing methods:

- It can generate composite models with volume fraction up to 50%, depending on the inclusion aspect ratio;
- Realistic microstructures can be produced by using specified distributions of inclusion geometries;
- It effectively uses the surface-to-surface based contact algorithm to prevent inclusion overlap instead of the computationally expensive iterative approach;
- The microstructure does not have any predefined gap between inclusions;
- The system is developed by integrating commercially available computer aided engineering tools, which facilitates the further extension and integration of this method with other systems.

The manuscript is organized as follows: a detailed description of different components of the proposed numerical system is presented in Section 2. Section 3 presents illustrative samples of the generated RVEs and a discussion on their geometrical features. In Section 4, we perform a microstructural characterization study by investigating randomness, homogeneity and isotropy of the generated RVEs.

## 2. Model generation framework

The proposed method for generating models with stochastic microstructure consists of three distinct components: (1) a sparse inclusion assembly generation step, (2) a packed inclusion assembly generation step, and (3) a step in which a CAD model of the problem domain is produced. The structure of this computational framework is illustrated in Fig. 1. The three steps are taken sequentially as suggested in the figure. This model generation concept is inspired from numerical optimization schemes developed in Refs. [20,21]. Details of the each system are discussed in the following sub-sections.

### 2.1. Sparse inclusion assembly generation

The objective of this step is to generate multiple sparse random inclusion assemblies with low volume fraction. These filler assemblies are generated using the RSA algorithm with an imposed minimum distance constraint between neighboring inclusions. We assume that inclusions have circular cross-section and model them as straight cylinders with a choice of aspect ratio and length. This assumption does not limit the applicability of the method to composites containing other types of inclusions. Inclusion axes are generated as line segments in a cubic box of size L, with random spatial position of their centers and random orientation. The dimension L coincides with that of the final, target model. For a fiber of length $l$, we first choose the position vector of one of its end points $\boldsymbol{P_0}$ as a random vector uniformly distributed on $[0, L]$ and two Euler angles $\theta$ and $\gamma$ as shown in Fig. 2.

To ensure uniform random orientation over a unit sphere, two random variables uniformly distributed on [0, 1], u and v, are used and then the angles are calculated as [22]:

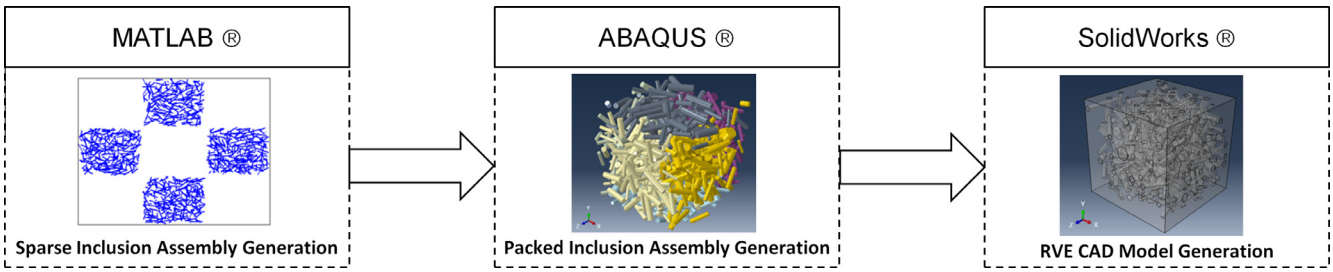


**Fig. 1.** Components of the stochastic model generation framework. The software tools used in each step are indicated.

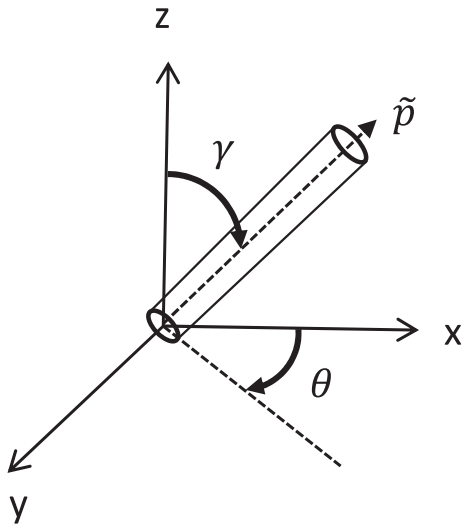


**Fig. 2.** Definition of two angles ($\theta$, $\gamma$) and orientation unit vector ($\tilde{p}$) of an inclusion.

$$\theta = 2\pi u \tag{1}$$

$$\gamma = \cos^{-1}(2v - 1) \tag{2}$$

Based on the two angles, the orientation unit vector $\tilde{\boldsymbol{p}}$ is determined. Then, the axis of the inclusion is generated by determining the other end point $P_1$ as:

$$\tilde{\boldsymbol{p}} = \cos\theta \sin\gamma \boldsymbol{e}_1 + \sin\theta \sin\gamma \boldsymbol{e}_2 + \cos\gamma \boldsymbol{e}_3 \tag{3}$$

$$\mathbf{P}_1 = \mathbf{P}_0 + l\tilde{\boldsymbol{p}}. \tag{4}$$

Each newly generated inclusion is defined based on its axis and is checked for intersection with others inclusions and with the box boundaries. If an inclusion crosses any box boundary face, it is cut at the boundary and the segment outside the box is transferred to the opposite face, while retaining its original orientation. This procedure is usually implemented to introduce periodicity at model boundaries. However, in our system, the periodicity is not preserved during the second step of the model generation in order to allow realistic random arrangements to be created both in the middle of the box and in the vicinity of the box boundary. This procedure helps us reduce the inclusion rejection rate due to boundary crossing.

Inclusion-to-inclusion intersection check is implemented by computing the minimum distance between two inclusion axes based on the algorithm proposed in Ref. [23]. It is based on the principle of closest point of approach (CPA) method. Zhou et al. [12] and Bailakanavar et al. [14] also implemented a similar algorithm for intersection checking. Pan et al. [18] formulated a linear two variable distance function for two arbitrary inclusion pairs and solved a constrained nonlinear optimization problem to determine the minimum distance between two inclusion. Although the CPA method is computationally more efficient than solving an optimization problem, the procedure is still computation intensive especially when the number of inclusions to be generated is sufficiently large. For example, to generate N inclusions, the number of intersections to be checked is N(N − 1)/2 as for each inclusion we need to check its intersections with all previously generated inclusions. To expedite the intersection checking process, we implemented a nearest neighbor search algorithm commonly used in machine learning and pattern recognition [24]. This algorithm identifies inclusions within a reasonable proximity of the target inclusion and then the CPA method is used to check inclusion intersections with the resulting set of neighboring inclusions.

A generated inclusion is accepted only when the shortest distance between its axis and the axis of any other inclusion is greater than the sum of their corresponding radiuses and the predefined minimum distance threshold. Otherwise, it is regenerated with a new random orientation and location. In the present implementation, the minimum distance threshold is set at 10% of the inclusion diameter. This loop is repeated until the desired inclusion volume fraction is achieved or the number of attempts to generate a new inclusion exceeds $\mathbf{10^6}$.

The RSA algorithm discussed so far has been implemented in MATLAB®. It is to be noted that at this stage, we only generate inclusion axes and consider the inclusion volume virtually in order to define the minimum distance between inclusion axes and to test intersections. A representative sample assembly of inclusion axes is illustrated in Fig. 3(a) and the corresponding pseudo volume inclusion assembly is shown in Fig. 3(b). Here, the cubic box contains 376 cylindrical inclusions with identical aspect ratio of 8 and volume fraction equals to 5%. The volume fraction of inclusions in this intermediate model is 1/6 of the desired volume fraction in the final model. If we target a volume fraction of ∼50%, the intermediate fraction of ∼8% can be easily achieved with the standard RSA algorithm.

### 2.2. Packed inclusion assembly generation

To generate the final model, the inclusions contained in 6 intermediate models (the "pseudo-boxes") of the type described in Section 2.1 are allowed to simultaneously flow into an empty cubic box of size L (the "target box"). The 2D projection of the 3D set-up for this step is shown schematically in Fig. 4. The target box which will eventually contain the final model is placed in the center and contains no inclusion at the beginning of this step. The six other boxes containing the configuration produced in the first step of the procedure (Section 2.1) are placed adjacent to the 6 faces of the target box. The six pseudo boxes are enclosed by rigid impenetrable surfaces (continuous red lines in Fig. 4) on all faces except the ones shared with the target box (dashed red lines in Fig. 4). These rigid surfaces guide inclusions into the target box. The transfer of inclusions from pseudo boxes into the target box

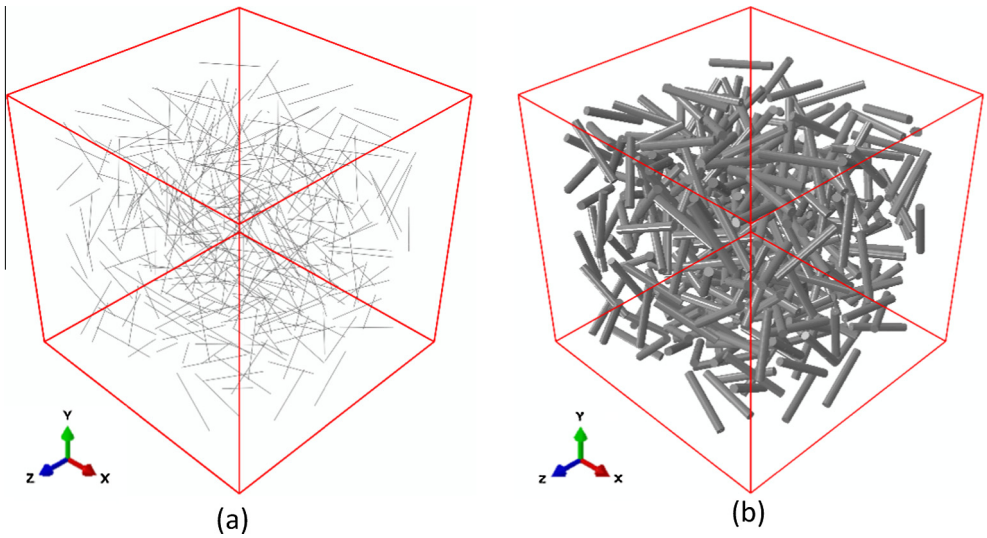


**Fig. 3.** Representative sparse inclusion assembly with (a) only inclusion axes shown and (b) with full inclusion volume shown.

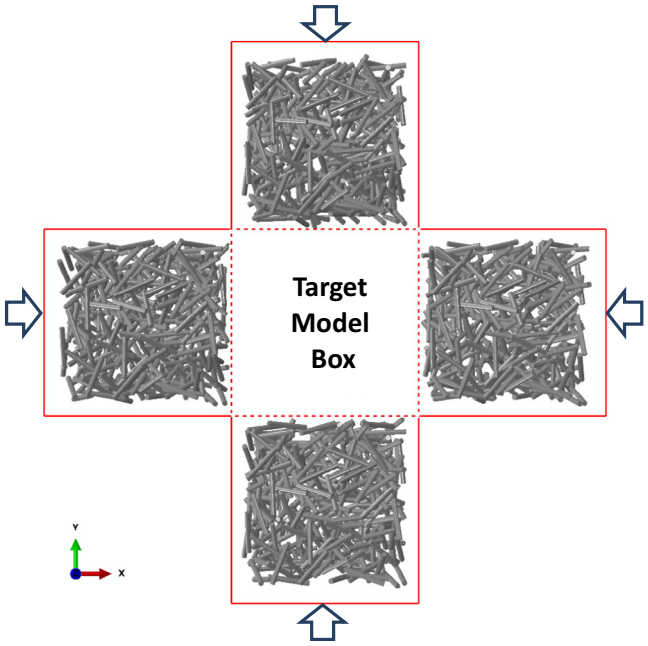


**Fig. 4.** 2D projection of the 3D set-up used to generate the model of high volume fraction. The target box shown in the middle contains no fillers at the beginning of this step. The lateral pseudo-boxes contain configurations produced in the first step of the procedure (Section 2.1). The dashed/continuous red lines are penetrable/impenetrable for moving inclusions. The arrows indicate the displacement direction of surfaces to which the arrows point. (For interpretation of the references to colour in this figure legend, the reader is referred to the web version of this article.)

is performed using Abaqus/Explicit as a dynamic simulation. We impose displacement boundary conditions on the rigid surfaces parallel to target box faces (shown by arrows in Fig. 4) such that all inclusions are guided simultaneously towards the target box. The dynamics of the process is controlled by choosing a sufficiently large simulation time in order to prevent high speed impact or crash of inclusions. A supplementary materials video demonstrating this procedure is provided.

Abaqus/Explicit is a robust FEM solver widely used to simulate transient dynamic events such as automotive crashworthiness or ballistic impact. To the best of authors' knowledge, there is no published report in the literature that utilizes dynamic FEM simulation for inclusion packing during composite model generation. The ability of Abaqus/Explicit to effectively handle a large number of contacts between surfaces makes it very attractive for this task [25]. In this work, we utilize this capability in order to generate stochastic composite models with high volume fraction of non-overlapping cylindrical inclusions.

For the dynamic FE simulation each inclusion is discretized in multiple 3D Timoshenko beam elements (element type B32 in Abaqus). Each element has three nodes and each node has six degrees of freedom - three transitional and three rotational. Modeling the inclusions as beam elements reduces the total number of degrees of freedom and the simulation time, allowing the representation of a large number of inclusions.

In order to prevent inclusion intersection during packing, we implemented surface based contact constraint between inclusions during the dynamic packing simulation. Specifically, we use the general contact algorithm in Abaqus [25]. El-Rahman et al. [26] also used the general contact algorithm to simulate compressive behavior of random fiber assemblies. The contact between two inclusion surfaces may occur in two directions- one normal to the surfaces and one tangential to the surfaces. To capture normal contact behavior, Abaqus requires the specification of a pressure-overclosure relationship. In our model, a 'hard' contact relationship is found to be the most suitable as it enforces zero penetration condition and allows any contact pressure to be transmitted between surfaces [25]. In addition, to model tangential contact behavior that induces relative sliding of inclusion surfaces, frictional interaction of inclusions is considered. This is modeled as Coulomb friction with a coefficient of friction $\mu = 0.3$.

We allow the solver to automatically choose the required stable time increment to achieve convergence. The solver approximates the minimum stable time in each increment based on the minimum element dimension and current dilatational wave speed in each element. We use a total physical simulation time of 10 s for which the minimum stable time increment is on the order of $10^{-4}$ to $10^{-5}$ depending on the aspect ratio. Furthermore, to capture the contacts between inclusion pairs accurately, it is also important to discretize the inclusions with sufficient number of elements. We observe that for inclusions with aspect ratio ($AR \leqslant 5$), one element per inclusion is sufficient if the desired volume fraction is relatively small ($\phi \leqslant 20\%$). However, for higher volume fractions, inclusions should be discretized with element aspect ratios smaller or equal to 3. This condition is related to the probability of having multiple contacts per inclusion. For higher aspect ratios ($AR > 5$), inclusions discretized with elements

of aspect ratio equals to 3 also provided satisfactory convergence up to volume fraction approximately 50%.

To avoid initial overlap between rigid surfaces and inclusions, a predefined clearance of 5% of the box length (L) is introduced as shown in Fig. 4. In addition, only the rigid surface placed on the opposite face of free face is displaced towards the target box. The displacement has been applied by means of a smooth amplitude curve to prevent excessive rotation of inclusions. The general contact algorithm automatically imposes contact constraint between rigid surfaces and inclusions and we specifically instruct the solver to exclude contacts between rigid surfaces by defining corresponding surface pairs. A representative 3D packed inclusion assembly is shown in Fig. 5(a) and the corresponding side view is shown in Fig. 5(b).

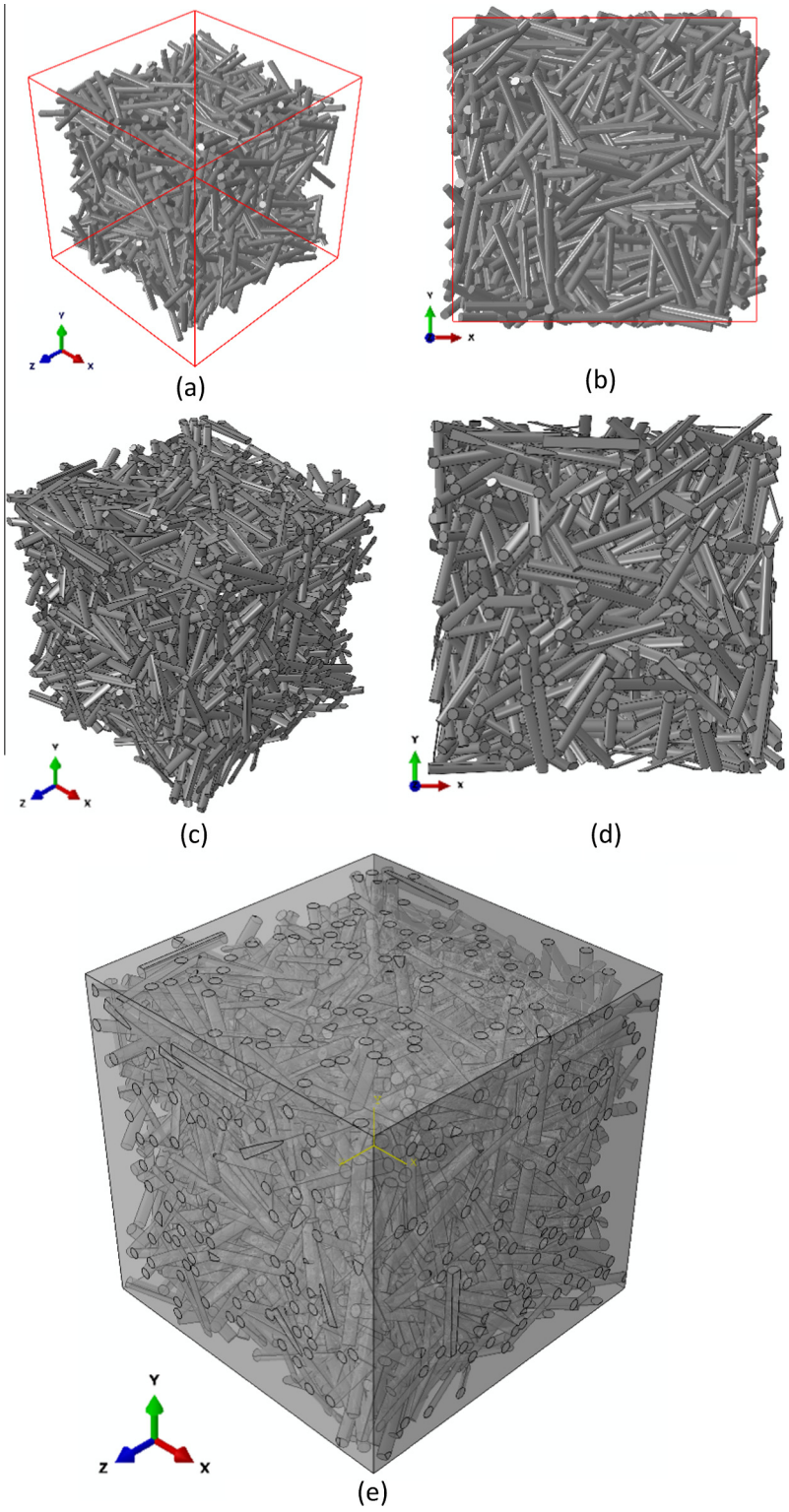


**Fig. 5.** (a) 3D packed inclusion assembly of 43% volume fraction, (b) side view of the configuration in (a), (c) 3D chopped inclusion assembly, (d) side view of the configuration in (c), and (e) final RVE with chopped fiber assembly embedded in matrix.

### 2.3. RVE CAD model generation

The packed fiber assembly contains inclusions in the form of beam elements that needs to be transformed into a 3D CAD model; which can be further used to perform numerical analysis of composite behavior. In this step, the 3D volume of a cylindrical inclusion is constructed by sweeping the circular cross-sectional fiber profile along the trajectory defined by the fiber centerline. While it is fairly straightforward to generate a CAD model of a single inclusion, the process becomes tedious when the number of inclusions is large. To automate the CAD modeling process, we have developed a SolidWorks API script within the VBA programming environment. The script automatically reads the inclusion coordinates from a text file and generates individual inclusions by solid sweeping. We found that inclusion distribution near the box boundary is relatively non-uniform. To eliminate such nonuniformity, the box is truncated by 2.5% of L from each edge. In addition, inclusions located in the close vicinity of the box faces are observed to create distorted or poorly shaped elements in the final model mesh. To address this problem these inclusions are removed in a post-processing step using a MATLAB code developed for this purpose.

Previous researchers have indicated the requirement of a minimum distance between inclusions in order to avoid the generation of distorted elements. Since the distance between inclusions is not explicitly controlled in the current algorithm, meshing the generated composite geometry may become a challenging task. In this study, we used Simmetrix Inc. meshing tool called MeshSim [27] for mesh generation. MeshSim has the capability to generate conforming meshes for multi-material models with several mesh sizes and mesh quality control attributes. Specifically, we used curvature based mesh refinement and curved mesh generation capabilities to ensure reasonable mesh quality. A discussion on mesh generation is beyond the scope of the current article; further details are presented in Refs. [28–30].

The CAD model of a representative chopped fiber assembly is shown in Fig. 5(c) and the corresponding side view is shown in Fig. 5(d). As the final step, we generate the matrix material by generating a cube of size L from which the inclusion assembly is subtracted through a Boolean operation. A representative CAD model with inclusions embedded in matrix is shown in Fig. 5(e).

## 3. Results and discussion

Three distinct types of models are generated to demonstrate the procedure described in Section 2:

- **Type I:** this model contains inclusions of identical aspect ratio. For demonstration purpose we select AR = 5, 8 and 10 in separate models.

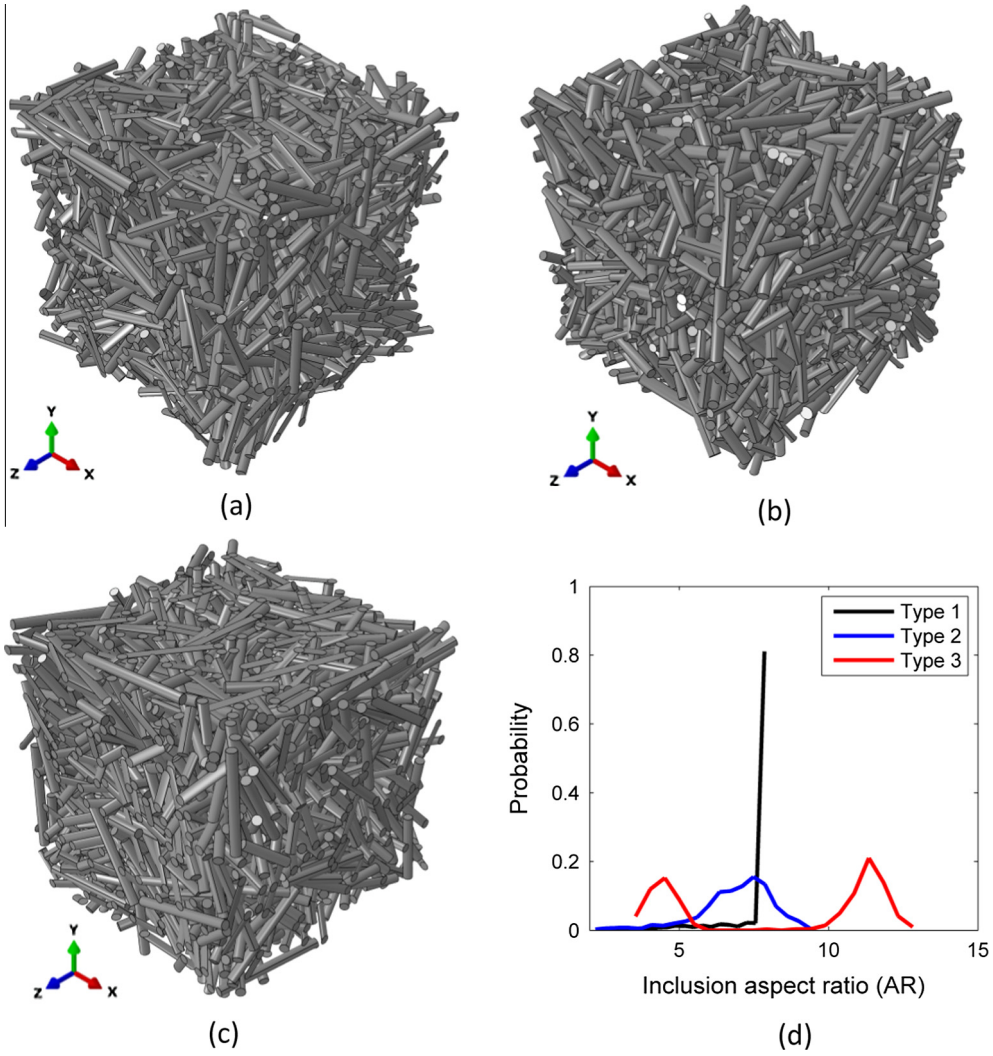


**Fig. 6.** Representative inclusion assemblies of models of (a) Type I ($\phi$ = 43%), (b) Type II ($\phi$ = 42.2%), (c) Type III ($\phi$ = 42.4%) and (d) the corresponding aspect ratio distributions.

**Table 1**
Characteristics of generated representative inclusion assembly samples.

| Sample # | Imposed aspect ratio (AR) | Number of inclusions ($n_I$) | Mean aspect ratio ($\overline{AR}$) | Std. deviation of aspect ratio ($\sigma_{AR}$) | Initial volume fraction ($\phi_0$, %) | Final volume fraction ($\phi$, %) |
|---|---|---|---|---|---|---|
| 1 | 5 | 867 | 4.699 | 0.672 | 4 | 39.9 |
| 2 | 5 | 971 | 4.650 | 0.726 | 5 | 44.3 |
| 3 | 5 | 1165 | 4.536 | 0.840 | 8 | 51.8 |
| 4 | 8 | 1603 | 7.550 | 1.101 | 4 | 38 |
| 5 | 8 | 1954 | 7.570 | 1.081 | 5 | 43 |
| 6 | 8 | 2490 | 7.196 | 1.491 | 8 | 52 |
| 7 | 10 | 1238 | 9.247 | 1.584 | 4 | 33 |
| 8 | 10 | 1501 | 8.435 | 2.303 | 5 | 36 |
| 9 | 10 | 1534 | 9.929 | 0.595 | 6 | 44.3 |
| 10 | $AR \sim N(\mu, \sigma^2)$ $5 \leqslant AR \leqslant 10$ | 1740 | 7.045 | 1.125 | 4 | 35 |
| 11 | | 2137 | 6.893 | 1.247 | 5 | 42.2 |
| 12 | | 2476 | 6.583 | 1.396 | 6 | 44.9 |
| 13 | $AR \sim N(\mu, \sigma^2)$ $3 \leqslant AR \leqslant 15$ (bi-modal dist.) | 1524 | 8.154 | 3.550 | 4 | 36.1 |
| 14 | | 1729 | 8.428 | 3.461 | 5 | 42.4 |
| 15 | | 1876 | 8.379 | 3.449 | 6 | 45.7 |

- **Type II:** this model contains inclusions with AR sampled from a truncated normal distribution of mean $\overline{AR} = 7.5$ and standard deviation $\sigma_{AR} = 0.83$. Note that 99.7% of the samples taken from this distribution are in the interval (5,10).
- **Type III:** this model contains inclusions with AR sampled from a bimodal distribution defined by two Gaussian peaks centered at 4.5 and 11.5, both with a coefficient of variation of 0.11, i.e. the standard deviation of the Gaussian centered at 4.5 is 0.5 while that of the Gaussian centered at 11.5 it is 1.26.

Representative inclusion assemblies of each model type are shown in Fig. 6.

### 3.1. Geometric characterization

Multiple samples have been generated for each type of microstructure. Table 1 shows the relevant parameters of all these composites. An initial volume fraction $\phi_0$ within the range 4–8% has been used to generate sparse inclusion assemblies using the RSA algorithm as described in Section 2.1. The number of inclusions in each model is specified in Table 1. Representative aspect ratio distributions for three types of samples are shown in Fig. 6 (d). The final packing reproduces the target AR distribution approximately. The error is due to the truncation of inclusions close to the boundaries. Columns 4 and 5 of Table 1 indicate the actual aspect ratio mean and standard deviation of each realization. The final volume fraction is also indicated.

For constant aspect ratio ($AR \leqslant 8$), the proposed method generates maximum volume fractions up to approximately 50%. For example, for aspect ratio AR = 5, the maximum volume fraction achieved is 51.8%. For aspect ratio AR = 10, we achieved a maximum volume fraction of 44.3%. On the other hand, a maximum volume fraction of 44.9% is achieved for composites of Type II having inclusions with broad distribution of AR values. For composites of Type III the maximum achieved volume fraction is 45.72%. These values are much larger than can be obtained with the conventional RSA algorithm.

The final volume fraction, $\phi$, is controlled by the initial volume fraction in the pseudo-boxes, $\phi_0$, by the inclusion aspect ratio and by the computational time of the dynamic simulation. We have found that for a given $\phi_0$, the final volume fraction, $\phi$, is approximately between $7\phi_0$ and $9\phi_0$. Note that in principle, the final volume fraction should be $6\phi_0$. The difference is introduced by the trimming of the model, which amounts to approximately 5% of the box length L, in order to eliminate the model boundaries which are more non-uniformly packed, as discussed above. More quantitatively, we have observed that for $\phi_0 \leqslant 5\%$ *and* $5 \leqslant AR \leqslant 10$, $\phi$ can be expressed in terms of $\phi_0$ and AR as:

$$\phi = 0.61\phi_0^3 - 6.7\phi_0^2 + 28\phi_0 - 8.6 + f(AR) \tag{5}$$

$$f(AR) = 0.37AR^2 + 4.3AR - 5.34 \tag{6}$$

Eq. (5) shows that the final volume fraction, $\phi$, is a third order polynomial function of $\phi_0$ with the constant term depending on the inclusion aspect ratio (AR) as defined by Eq. (6). A comparison of the measured $\phi$ for different combination of control parameters ($\phi_0$, $AR$) with the prediction of Eq. (5) is shown in Fig. 7.

A sufficiently small time step and refined mesh are required to capture the contacts between inclusion surfaces at arbitrary locations during the dynamic simulation. This increases the computation time considerably. Since model generation should be rather fast (the generation of all models discussed in this article require less than 30 min on a 2.60 GHz Intel® Core), one should consider selecting reasonable simulation time and time increment for this step. As discussed in Section 2.2, a simulation time of 10 s and time increment on the order of $10^{-4}$ to $10^{-5}$ was observed to be optimum for current work.

### 3.2. Statistical characterization

We perform a detailed statistical characterization of the samples listed in Table 1 in order to demonstrate the capability of

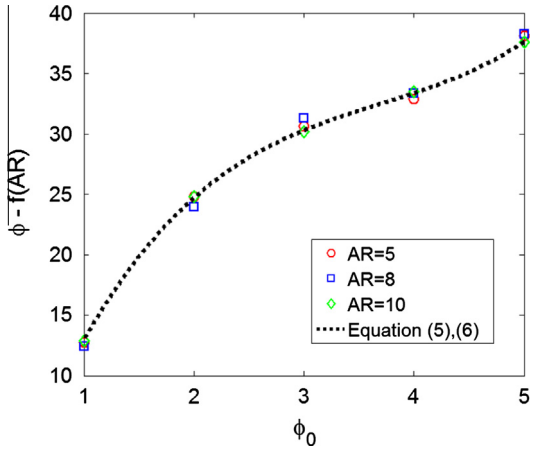


**Fig. 7.** Dependence of the final volume fraction, $\phi$, on the initial volume fraction, $\phi_0$, and the inclusion aspect ratio (AR). Symbols indicate $\phi$ resulting from the actual simulations and the dotted line represents the predictions of Eq. (5).

the proposed method to generate models with random orientation of inclusions and with small spatial variability of the filling fraction evaluated over sub-domains.

**Isotropy:** to evaluate the isotropy of the microstructures we calculated the orientation order parameter (Herman's orientation function) $P_2$, which is one of the diagonal entries of the orientation tensor:

$$P_2 = \frac{1}{2}\langle 3\cos^2\alpha - 1\rangle \tag{7}$$

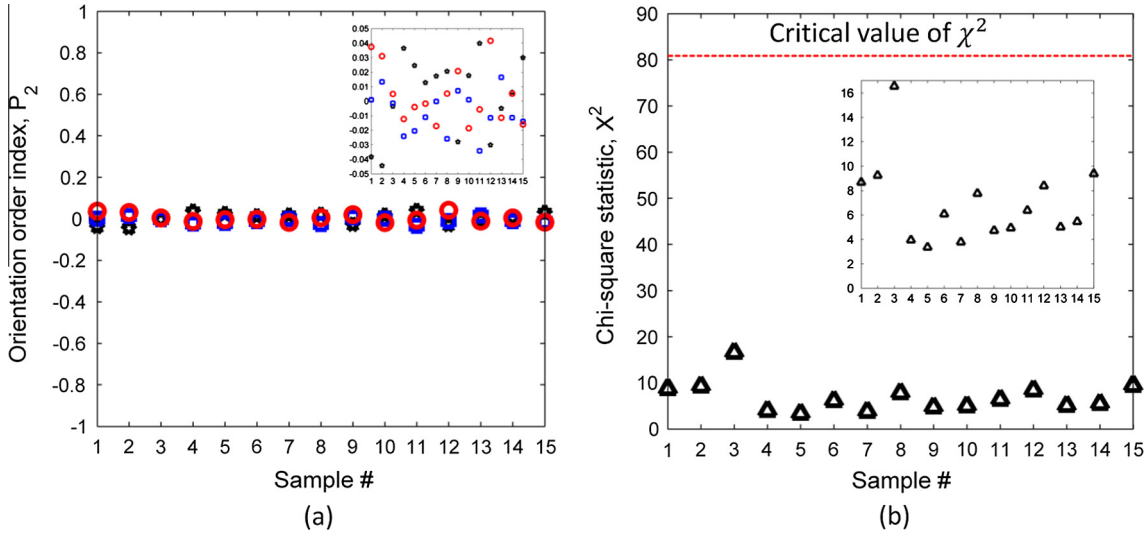


**Fig. 8.** Statistical parameters for all samples listed in Table 1: (a) orientation order index $P_2$ with respect to the X axis (black star), Y axis (blue square), and Z axis (red circle) and (b) chi-square statistic ($\chi^2$). The insets show the zoom-in view of the data in the main figure. (For interpretation of the references to colour in this figure legend, the reader is referred to the web version of this article.)

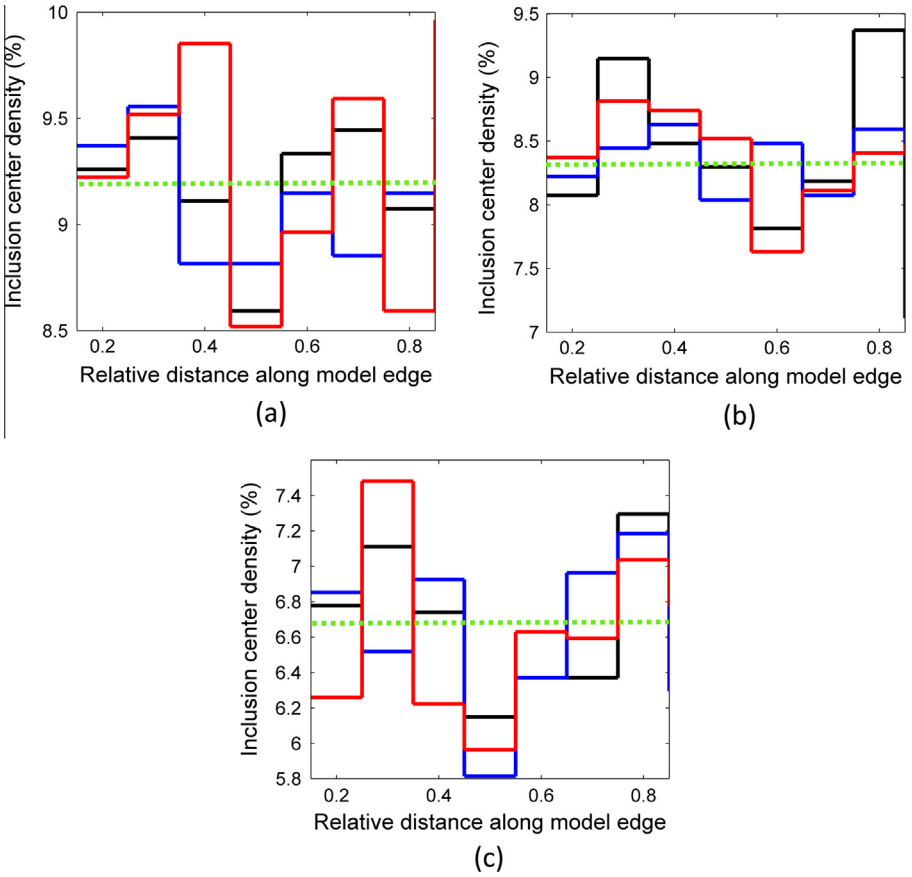


**Fig. 9.** Representative inclusion center density distributions for: (a) Type I (sample #6), (b) Type II (sample #11) and (c) Type III (sample #14). The black, blue and red solid lines correspond to distributions for binning along the X, Y and Z axes respectively. The horizontal axis shows the position along the respective axis normalized by the model size, L. The green dashed lines show the average density of the models. (For interpretation of the references to colour in this figure legend, the reader is referred to the web version of this article.)

Here, $\alpha$ is the angle between a specified direction and the long axis of a cylindrical inclusion and $\langle\rangle$ indicates ensemble averaging of the respective quantity over the population of inclusions. This parameter takes values of 0, 1 and $-1$ for randomly oriented assemblies of vectors, and for perfect alignment in the parallel and perpendicular directions to the reference axis, respectively. We compute $P_2$ with respect to the three global coordinate axes X, Y and Z. For all cases, the calculated values are less than 0.1, which indicates that the inclusion distribution is isotropic. Fig. 8(a) shows $P_2$ values for several samples.

**Homogeneity:** to examine the homogeneity, we apply the chi-square statistical hypothesis test as implemented by He et al. [31]. We divide the box into 64 equal cubic sub-domains and compute the volume fraction of inclusions in each such sub-domain. Then, the validity of the hypothesis that the inclusions are uniformly distributed is tested by calculating the $\chi^2$ statistics:

$$\chi^2 = \sum_{i=1}^{i=k} \frac{(O_i - E_i)^2}{E_i} \tag{8}$$

where $O_i$ is the observed density value in subregion i, $E_i$ is the expected density value in subregion i and k is the total number of subregions in the given model. According to the $\chi^2$ test, the hypothesis is to be rejected if the calculated value is greater than the critical value for a given significance level ($\alpha$). At $\alpha = 0.05$ level, the critical value is $\chi^2_{0.05,63} = 82.53$ for 63 degrees of freedom [32]. The calculated $\chi^2$ values are much smaller than the critical value for all samples, as shown in Fig. 8(b). This implies that the inclusion distribution is homogenous.

In addition, the homogeneity of the inclusion distribution is tested by computing the distribution of inclusions centers. For this purpose, the model is divided in 10 equal sized bins of width L/10, and the number of inclusion centers in each bin is calculated. Representative inclusion center density (number of inclusion centers per unit bin volume) distributions along the three coordinate directions are shown in Fig. 9. As shown, the distribution is sufficiently uniform throughout the model volume, with small variability of approximately 10% with respect to mean model density. It is to be noted that larger density fluctuations are introduced near the model boundaries as we have intentionally removed some inclusions located close to the boundaries in order to facilitate meshing of the model in the last step of the model generation procedure. These boundary layers can be easily trimmed, as a final step of the process.

## 4. Conclusion

A novel computational tool for generating models of stochastic composites has been developed. The presented method efficiently uses dynamic FE simulations to produce models of high volume fraction and broad inclusion aspect ratio distribution. The method is more efficient than the standard RSA algorithm, especially for higher volume fractions. The performance of the developed tool has been demonstrated by generating several models for different inclusion aspect ratio distributions.

The resulting models are isotropic and homogeneous. To demonstrate this, the orientation index of inclusions axes as well as the $\chi^2$ test are used to evaluate three types of composites: Type I models containing inclusions of identical aspect ratio, Type II composites containing inclusions with aspect ratio sampled from a truncated Gaussian distribution, and Type III models with inclusions have aspects ratios sampled from a bi-modal distribution. These measures indicate the isotropy and homogeneity of the resulting models. Therefore, the method can be used to generate representative volume elements of stochastic composites with minimal dimensions.

Furthermore, the method can be extended to generate models of composites with inclusions of other shapes, such as ellipsoids and spheres, by representing the inclusions in the first step of the method as two dimensional surface elements in lieu of beam elements.

## Acknowledgement

This material is based on the work supported by National Science Foundation (NSF) under Grant No. 1362234.

## Appendix A. Supplementary material

Supplementary data associated with this article can be found, in the online version, at http://dx.doi.org/10.1016/j.commatsci.2016.08.051.

## References

[1] G. Dvorak, Micromechanics of Composite Materials, Springer Science & Business Media, 2012.
[2] S. Nemat-Nasser, M. Hori, Micromechanics: Overall Properties of Heterogeneous Materials, Elsevier, 2013.
[3] S. Torquato, Random Heterogeneous Materials: Microstructure and Macroscopic Properties, Springer Science & Business Media, 2013.
[4] T. Mori, K. Tanaka, Average stress in matrix and average elastic energy of materials with misfitting inclusions, Acta Metall. 21 (1973) 571–574.
[5] J.D. Eshelby, The determination of the elastic field of an ellipsoidal inclusion, and related problems, in: Proceedings of the Royal Society of London A: Mathematical, Physical and Engineering Sciences, The Royal Society, 1957, pp. 376–396.
[6] R. Christensen, F. Waals, Effective stiffness of randomly oriented fibre composites, J. Compos. Mater. 6 (1972) 518–535.
[7] H. Cox, The elasticity and strength of paper and other fibrous materials, Br. J. Appl. Phys. 3 (1952) 72.
[8] S.G. Advani, C.L. Tucker III, The use of tensors to describe and predict fiber orientation in short fiber composites, J. Rheol. (1978-present) 31 (1987) 751–784.
[9] J. Halpin, N. Pagano, The laminate approximation for randomly oriented fibrous composites, J. Compos. Mater. 3 (1969) 720–724.
[10] N. Chawla, R. Sidhu, V. Ganesh, Three-dimensional visualization and microstructure-based modeling of deformation in particle-reinforced composites, Acta Mater. 54 (2006) 1541–1548.
[11] R. Hill, Elastic properties of reinforced solids: some theoretical principles, J. Mech. Phys. Solids 11 (1963) 357–372.
[12] J. Zhou, L. Qi, A.M. Gokhale, Generation of three-dimensional microstructure model for discontinuously reinforced composite by modified random sequential absorption method, J. Eng. Mater. Technol. 138 (2016) 021001.
[13] Y. Pan, L. Iorga, A.A. Pelegri, Analysis of 3D random chopped fiber reinforced composites using FEM and random sequential adsorption, Comput. Mater. Sci. 43 (2008) 450–461.
[14] M. Bailakanavar, Y. Liu, J. Fish, Y. Zheng, Automated modeling of random inclusion composites, Eng. Comput. 30 (2014) 609–625.
[15] S. Kari, H. Berger, R. Rodriguez-Ramos, U. Gabbert, Computational evaluation of effective material properties of composites reinforced by randomly distributed spherical particles, Compos. Struct. 77 (2007) 223–231.
[16] H.J. Böhm, A. Eckschlager, W. Han, Multi-inclusion unit cell models for metal matrix composites with randomly oriented discontinuous reinforcements, Comput. Mater. Sci. 25 (2002) 42–53.
[17] S. Kari, H. Berger, U. Gabbert, Numerical evaluation of effective material properties of randomly distributed short cylindrical fibre composites, Comput. Mater. Sci. 39 (2007) 198–204.
[18] Y. Pan, L. Iorga, A.A. Pelegri, Numerical generation of a random chopped fiber composite RVE and its elastic properties, Compos. Sci. Technol. 68 (2008) 2792–2798.
[19] L.T. Harper, C. Qian, T.A. Turner, S. Li, N.A. Warrior, Representative volume elements for discontinuous carbon fibre composites – Part 1: boundary conditions, Compos. Sci. Technol. 72 (2012) 225–234.
[20] M. Islam, A. Buijk, M. Rais-Rohani, K. Motoyama, Process parameter optimization of lap joint fillet weld based on FEM–RSM–GA integration technique, Adv. Eng. Softw. 79 (2015) 127–136.
[21] M. Islam, A. Buijk, M. Rais-Rohani, K. Motoyama, Simulation-based numerical optimization of arc welding process for reduced distortion in welded structures, Finite Elem. Anal. Des. 84 (2014) 54–64.
[22] E.W. Weisstein, Sphere Point Packing, in: MathWorld–A Wolfram Web Resource.
[23] S. Dan, Distance between Lines, Segments and the Closest Point of Approach (2D & 3D), 2001.
[24] T.M. Cover, P.E. Hart, Nearest neighbor pattern classification, IEEE Trans. Inform. Theory 13 (1967) 21–27.

[25] Abaqus 6.13 Documentation, 2013.
[26] A.A. El-Rahman, C. Tucker III, Mechanics of random discontinuous long-fiber thermoplastics. Part II: direct simulation of uniaxial compression, J. Rheol. (1978-present) 57 (2013) 1463–1489.
[27] http://www.simmetrix.com/products/SimulationModelingSuite/MeshSim/MeshSim.html.
[28] X. Li, M.S. Shephard, M.W. Beall, Accounting for curved domains in mesh adaptation, Int. J. Numer. Meth. Eng. 58 (2003) 247–276.
[29] M.W. Beall, M.S. Shephard, A general topology-based mesh data structure, Int. J. Numer. Meth. Eng. 40 (1997) 1573–1596.
[30] M.S. Shephard, Meshing environment for geometry-based analysis, Int. J. Numer. Meth. Eng. 47 (2000) 169–190.
[31] D. He, N. Ekere, L. Cai, Computer simulation of random packing of unequal particles, Phys. Rev. E 60 (1999) 7098.
[32] https://en.wikibooks.org/wiki/Engineering_Tables/Chi-Squared_Distibution.